Journal of Non-Crystalline Solids 452 (2016) 320–324

Contents lists available at ScienceDirect

Journal of Non-Crystalline Solids

journal homepage: www.elsevier.com/locate/jnoncrysol

Electron Paramagnetic Resonance (EPR) studies on the photo-thermo ionization process of photo-thermo-refractive glasses

Claudio José Magon [a,*], José Pedro Donoso Gonzalez [a], José Fernando Lima [a], Hellmut Eckert [a,*], Edgar D. Zanotto [b], Julien Lumeau [c], Larissa Glebova [d], Leonid Glebov [d]

[a] Instituto de Física de São Carlos, Universidade de São Paulo, São Carlos, SP 13.566-590, Brazil
[b] Laboratório de Materiais Vítreos (LaMaV), Departmento de Engenharia des Materiais (DEMa), Universidade Federal de São Carlos (UFSCar), 13.565-905 São Carlos, SP, Brazil
[c] Aix Marseille Univ., CNRS, Centrale Marseille, Institut Fresnel, Marseille, France
[d] CREOL, College of Optics and Photonics, University of Central Florida, Orlando, FL 32816, USA

ARTICLE INFO

Article history:
Received 19 May 2016
Received in revised form 15 September 2016
Accepted 18 September 2016
Available online xxxx

Keywords:
Photo-thermo-refractive
Glass
EPR spectroscopy
Crystallization
PTR

ABSTRACT

Photo-thermo-refractive (PTR) glass is an optically transparent photosensitive sodium alumino silicate glass, containing NaF and KBr additives, along with cerium, silver, tin and antimony oxide dopants. UV-exposed regions of this glass produce NaF nanocrystals upon heating, giving rise to a permanent localized refractive index change. In this article we examine the initial stages of this crystallization process by continuous-wave and pulsed X-band electron paramagnetic resonance (EPR) spectroscopy. UV exposure of PTR glass produces unpaired electrons whose EPR spectrum is characterized by pronounced peak splitting arising from nuclear magnetic hyperfine interactions with spin-5/2 and spin-7/2 nuclei suggesting close proximity of the unpaired electrons with ^{121}Sb and ^{123}Sb nuclei. These results indicate that the Sb_2O_3 dopant plays a key role in the initial stages of the crystallization mechanism. Upon thermal annealing, leading to the crystallization of NaF, these species disappear, indicating their transient nature. A number of other unpaired electron species identified in the dopant free matrix appear to be unrelated to the crystallization process. These results clearly challenge the classical mechanism proposed decades ago to explain the complex crystallization process of PTR glass. Together with more recent results from optical spectroscopy they support the Nikonorov model involving (1) photoionization of Ce^{3+}, (2) transfer of this electron to Sb^{5+} species to create a Sb^{4+} species, (3) upon annealing electron transfer from Sb^{4+} to Ag^{+} ions, producing silver atoms, (4) coalescence of these species into Ag clusters, which (5) serve as nucleation catalysts for NaF nanocrystals.

1. Introduction

Photo-thermo refractive (PTR) glass is a photosensitive silicate glass whose optical properties can be modified in a controlled fashion by UV-exposure and subsequent annealing near the glass transition temperature, T_g. The chemical composition of a typical PTR glass is 15 Na_2O - 4 Al_2O_3 - 70 SiO_2 - 5 NaF - 5 ZnO - 1 KBr, with trace amounts (~0.01 mol.%) of the dopants Ce, Ag, Sb and Sn. By exposing glass samples to UV irradiation followed by adequate heat treatment, crystallization of NaF can be induced. Spatially patterned irradiation schemes afford glass-ceramics with periodically modulated indices of refraction, which are suitable for various photonic applications (generation of holograms, spectral and spatial filtering, and production of Bragg gratings) [1–4]. Devices of this kind are currently commercialized by a number of companies. The refractive index variations have been commonly postulated to arise from the formation of NaF nanocrystals in the UV-exposed areas of the sample upon annealing whose presence in the glass-ceramic has been detected by X-ray powder diffraction and solid state NMR [5]. For this reason many experimental studies have been devoted to elucidating the mechanism of NaF crystallization, dominantly using classical (macroscopic) examination methods [1–9]. However, it must be emphasized that there is – as of yet – only weak, indirect evidence linking the NaF crystals to the physical phenomenon of the refractive index variation. It is well-known that Ce^{3+} ions in glasses can be photo-ionized by UV irradiation and that the released electron can be trapped by an intrinsic defect or by an ion of a polyvalent element [10]. Initially it had been postulated that the main trapping mechanism is expected to be the formation of atomic Ag species, according to the reaction scheme [6–8]:

$$Ce^{3+} + Ag^{+} \rightarrow Ce^{4+} + Ag \quad (1)$$

Upon heating near the glass transition temperature, these Ag species are considered to form silver containing nanoparticles that serve as catalysts for the nucleation of NaF nanocrystals. The formation of these

* Corresponding authors.
E-mail address: eckerth@uni-muenster.de (H. Eckert).

http://dx.doi.org/10.1016/j.jnoncrysol.2016.09.012
0022-3093/

nanoparticles has been confirmed by a plasmon resonance broadband absorption centered at about 465 nm [11]. However, the special selective crystallization is known to proceed only in the presence the Sb and Sn dopants and the KBr additive, whose role in the crystallization process is not at all clear.

To obtain more specific structural information about the role of these dopants at the atomic level, suitable spectroscopic techniques are required. A wide range of optical spectroscopic studies have been carried out recently. For example Anne et al. studied the structure of cerium ions in PTR glass matrix [12]. They showed that even if the two absorption bands of Ce^{3+} and Ce^{4+} species are overlapped in the UV spectral region, their spectra can be decorrelated and decomposed into individual Gaussian bands (two for each type of ion). This study was then completed by Efimov et al. who studied the structure of the intrinsic absorption tail of glass matrix and impurities in UV [13] but also proposed a more complex and accurate model for the cerium absorption in UV range based on 3 elementary Gaussian bands for each ion [14]. Finally, additional optical spectroscopic work on silver ion exchanged PTR glass corroborated the suggestion that the photo-thermo-induced process mechanisms are more complex than that shown by Eq. (1) and that, similarly to polychromatic glasses [2], additional ions, such as antimony, may be involved in these photo-thermo-induced processes [15]. However, due to the overlap of the absorption bands of the active species (cerium, silver, antimony, glass matrix, impurities such as iron, color centers), the analysis of optical spectroscopic curves is a very challenging task and the results are subject to a large uncertainty.

Despite the fact that several of the postulated species involved in the proposed reaction mechanisms (Ce^{3+}, atomic silver and small $Ag_n^{(n-1)+}$ clusters, Sb^{5+} species trapping an electron) carry unpaired electrons, to the present date no studies by electron paramagnetic resonance (EPR) have been carried out on this system. In this contribution we present, for the first time, results from continuous-wave and pulsed EPR spectroscopic measurements in order to characterize the mechanisms of photo-thermo-induced ionization that precede the crystallization process and the appearance of desired localized refractive index change. By varying their dopant compositions we have identified the various types of paramagnetic species formed during this process and characterized them according to their spin Hamiltonian parameters. Furthermore the observation (or absence) of nuclear magnetic hyperfine couplings in the EPR spectra can provide evidence for (or against) the involvement of the various different dopants in the ionization and nucleation process. Our results offer new evidence for the key role of the antimony oxide dopant in PTR glasses.

2. Experimental

2.1. Sample preparation and characterization

Table I summarizes the samples investigated in the present study. Samples were prepared according to previously published protocols [4]. The powdered starting materials Na_2CO_3, Al_2O_3, SiO_2, NaF, ZnO, KBr, Ce_2O_3, Ag_2O, Sb_2O_3, and SnO_2 were melted at 1450 °C for 120 min in a platinum crucible (typical batch size 500 g), and subsequently cooled to room temperature at a rate of 0.1 K/s. Light exposure was done using either a Xenon lamp or a He-Cd laser (wavelength 325 nm) under the conditions specified in Table 1. Table 2 summarizes the glass composition of samples B5 and B6, according to chemical analysis. Samples B1 and B2 have the same base compositions, but were prepared without the dopants Ce_2O_3, Ag_2O, Sb_2O_3, and SnO_2 while in the samples B3 and B4 Ag_2O was the sole dopant species present. X-ray powder diffraction confirmed that all the untreated samples were amorphous, as expected. Following this preparation step, some samples were annealed at 450 °C for 2 h, to induce nucleation of silver clusters and NaF.

Table 1
Compositions and treatment of the samples under study.

Sample	Dopant composition	Light exposure
B1	None	None
B2	None	20 min, Xe lamp [16]
B3	Ag_2O	None
B4	Ag_2O	20 min, Xe lamp [16]
B5	Ce_2O_3, Ag_2O, Sb_2O_3, SnO_2	None
B6	Ce_2O_3, Ag_2O, Sb_2O_3, SnO_2	He-Cd laser (325 nm), 10 J/cm^2 [17]

2.2. EPR spectroscopy

Continuous wave and pulsed EPR experiments were carried out in an E-580 BRUKER ELEXIS X-band EPR spectrometer operating at a microwave frequency around 9.5 GHz. The temperature was controlled by continuous flow liquid helium cryostats ESR-900 (cw) and CF-935 (pulsed) and PID controller from Oxford Instruments ITC503. CW measurements were performed at 30 K and pulsed experiments at 10 K. All samples were broken into small pieces to fit the bottom of a 3 mm inner diameter quartz tube used as a sample holder. The echo-detected field-sweep absorption spectra, EDFS, were recorded using a two-pulse echo sequence (π/2)-τ-(π)-τ-echo with a typical π/2 pulse width of 8 ns and repetition time of 2 ms. The pulse spacing, τ, was set long enough to suppress modulation effects and the integrated echo intensities were measured as a function of the magnetic field strength over the range of 0.1–12.1 kG. Spectral simulations were done by the function "*pepper*" of the software package EasySpin® implemented in MATLAB (MathWorks, Inc) [18]. The simulations consider the static spin Hamiltonian for electron-nucleus spin pairs in the solid state, given by

$$\mathcal{H} = \beta_e \boldsymbol{H}\cdot\boldsymbol{g}\cdot\boldsymbol{S} + \sum_j \boldsymbol{S}\cdot\boldsymbol{A}\cdot\boldsymbol{I}_j, \quad (2)$$

where the summation extends over the nuclear species considered in the simulation. In this expression the symmetric tensor $\boldsymbol{g}$, with its principal values g_{xx}, g_{yy} and g_{zz}, describes the anisotropic interaction of the electron spins $\boldsymbol{S}$ with the external magnetic field $\boldsymbol{H}$, while the tensor $\boldsymbol{A}$ describes the anisotropic magnetic hyperfine interaction between the electron spins and the nuclear spins $\boldsymbol{I}$ present. In the case of glassy systems we find a distribution the principal values for g and A, therefore, strain parameters were used to represent the disorder found in glasses. These strain parameters characterize Gaussian distribution functions of the g- and the A- parameters, resulting in field-dependent (g-strain) and field-independent (A-strain) line-broadening effects in the spectra [18]. Euler angles describing the orientation of g- and A-tensors relative to the molecular frame are considered all zero (coincident tensors). Table 3 summarizes the lineshape components and their corresponding Hamiltonian parameters.

Table 2
Precise chemical composition of the PTR glasses B5 and B6, according to chemical analysis.

NPTR glass composition	Wt.%	Mol.%
SiO_2	68.5	71.127
Al_2O_3	4.8	2.924
Na_2O	12.9	12.987
ZnO	6.6	5.100
NaF	4.3	6.362
KBr	2.8	1.457
Ag_2O	0.02	0.0062
CeO_2	0.02	0.0072
Sb_2O_3	0.10	0.021
SnO_2	0.02	0.0082
		Mol. weight
		62.4

Table 3
EPR simulation parameters extracted from the spectra. Electron spin is 1/2 in all cases. *Lwpp* is the line width for isotropic broadening used for convolution of the CW-EPR spectrum. Peak-to-peak (pp) refers to the horizontal distance between the maximum and the minimum of a first-derivative lineshape. The first and second entry of *lwpp* specifies Gaussian and Lorentzian broadening, respectively. *A*- and *g*-strain specifies the width of the Gaussian distribution of *A*- and *g*-values. For components 1, 2, 3 and $^{121/123}$Sb the uncertainty of *g* is ±0.0005; in the other cases it is ±0.01.

Sample	Spectral component	*g*	*g*-Strain ±5%	*A* (MHz) ±2%	*A*-strain (MHz) ±5%	*Lwpp* (MHz) ±1%
B2, B4	1	2.0053	–	–	–	1.5, 0
	^{23}Na or $^{79/81}$Br	2.41	–	820	380	1.0, 0
		2.20		450	220	
		1.91		660	200	
	^{27}Al	2.39	–	794	220	2.5, 0
		2.12		0	0	
		2.04		650	89	
B5	3	1.9063	–	–	–	4.0, 0.6
	2	1.9969	0.003	–	–	0.2,
		1.9869	0.009			0.3
		1.9835	0.004			
B6	3	1.9062	–	–	–	0.7, 5.0
	2	1.9972	0.004			0.2,
		1.9851	0.008			0.3
		1.9836	0.004			
	$^{121/123}$Sb	1.9169	–	^{121}Sb:1427 ^{123}Sb:772.7	^{121}Sb:360 ^{123}Sb:195	0, 4.5

3. Results and discussion

Figs. 1 and 2 give an overview of the experimental cw- and EDFS-EPR spectra of the samples under study. Comparing the two Figures, the complementary character of the two signal detection modes becomes very evident: while the continuous-wave method is the superior one for recording and resolving the narrower spectral features, the detection of very wide spectral patterns is only possible using the EDFS method. For example, the broad EPR lineshape attributed to the Ce^{3+} ions present in samples B5 and B6 can only be detected by the EDFS method. The lineshape of this broad signal arises from the $^2F_{5/2}$ ground state of the Ce^{3+} ions, and is probably influenced by both an anisotropic zero-field splitting compounded by an anisotropic *g*-tensor. Broad and poorly resolved lineshapes of this kind have been observed for various Ce^{3+} doped glasses and tentative analyses in terms of spin Hamiltonian parameters have been discussed in the literature, even though considerable uncertainty remains regarding the correct theoretical description [19–23]. We refrain from explicit simulation attempts of this component, which remained unchanged after UV irradiation and subsequent thermal annealing steps.

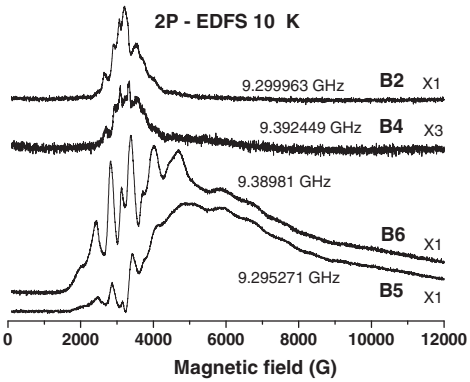

Fig. 2. Echo detected field sweep X-band EPR spectra obtained at 10 K on samples B2, B4, B5, and B6. Microwave frequencies are indicated.

No EPR signals are obtained on the unexposed glass matrix (sample B1) and the unexposed sample doped only with Ag (sample B3) in either experiment. These results clearly indicate that UV exposure is crucial for the formation of unpaired electron species. Therefore, we attribute mechanistic significance with relevance to the PTR process to only those paramagnetic species that are newly formed under the stated photo-treatment conditions when all of the dopants are present. Nevertheless, some paramagnetic species are also generated upon the UV-exposure of the dopant-free glass matrix itself (sample B2) and in the one exclusively doped with Ag (sample B4). The spectra obtained on these two samples are essentially identical, containing a very sharp singlet near $g = 2.0053$ ("component 1"), and a complex peak pattern which may reflect an unpaired electron with an anisotropic g-tensor and an anisotropic magnetic hyperfine interaction with a spin >1/2 nucleus. The sharp feature can be assigned with an oxygen defect species as has been frequently observed in irradiated silicate glasses [19]. For the remaining complex peak pattern, two possible simulations are shown in Fig. 3, however, it must be pointed out that there are many alternate ways of analysis. The peak manifold associated with this species may reflect hyperfine coupling of the unpaired electron with either a spin-3/2 species (^{23}Na or $^{79/81}$Br) or a spin-5/2 species (^{27}Al), or even both. As the spectra observed in samples B2 and B4 are essentially identical, we conclude that they reflect the same kind of unpaired electron species. Since both samples only differ with respect to the presence (absence) of the Ag dopant, we can exclude the possibility that these spectral features originate from any unpaired electrons associated with silver atoms or

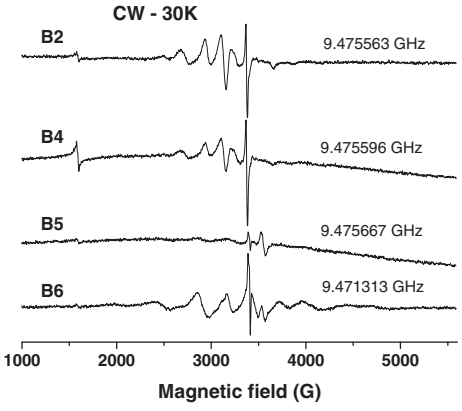

Fig. 1. Continuous wave X-band EPR spectra obtained at 30 K on samples B2, B4, B5, and B6. The sharp signal at 1593 G is attributed to Fe^{3+} impurities. Microwave frequencies are indicated.

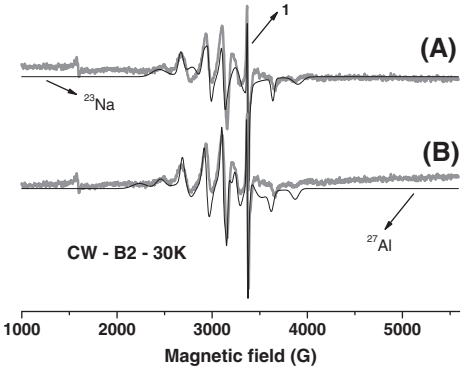

Fig. 3. Experimental cw spectrum of sample B2 (gray traces) and simulations (black traces). (A) Simulation with isotropic component 1 and hyperfine coupling to one spin-3/2 nucleus (^{23}Na or $^{79/81}$Br). (B) Simulation with isotropic component 1 and hyperfine coupling to one spin-5/2 nucleus (^{27}Al). The sharp signal at 1593 G is attributed to Fe^{3+} impurities. Microwave frequency: 9.475563 GHz.

clusters. While the nature of these unpaired electron species cannot be clarified at the present stage, it is important to note that these species are not observed in the spectrum of the UV-exposed fully doped sample. We thus conclude that they are of little relevance with respect to the mechanistic details of the photothermal refractive glasses.

Fig. 4 shows the simulation of the narrow features observed in the spectrum of the fully doped unexposed sample, B5, revealing two singlets near $g = 1.9891$ and 1.9063 ("components 2 and 3", respectively). The former one represents an unpaired electron with a small g-anisotropy, while the latter one can be described by an isotropic g-tensor. The same species are present in the UV-exposed photothermorefractive glass, sample B6, in which the intensity of component 2 is greatly enhanced. The absence of nuclear hyperfine splittings suggests that these signals arise from unpaired electrons located on oxygen atoms as reported in silica-based glasses [19,24,25]. The most striking feature of sample B6, however, is a complex multiplet centered near $g = 1.9169$. This species is characterized by strong magnetic hyperfine splitting revealing the interaction with the two nuclear isotopes ^{121}Sb (spin-5/2) and ^{123}Sb (spin-7/2). The spectrum shows very close resemblance to that observed by Schreurs and Davis in UV-exposed alkali silicate glasses containing small amounts of Sb_2O_3 and Ce^{3+} dopants [26]. The formation of Sb^{4+} in glasses upon UV or gamma-irradiation has also been briefly reported by other authors [27,28]. Fig. 5 shows the simulation of our experimental spectra, assuming an isotropic hyperfine interaction for simplicity. The constants $A_{iso} = 1427$ MHz (^{121}Sb) and 772.7 MHz (^{123}Sb) are very close to those observed in reference [26]. For optimal fitting of these spectra, a Gaussian distribution of magnetic hyperfine couplings must be assumed, reflected in the A-strain parameter (full width at half height of the distribution). Close inspection of Figs. 1 and 2 indicates further that the unexposed sample B5 contains some Sb^{4+} albeit with much reduced intensity. We attribute this observation to photo-activation by the UV component present in the spectrum of ambient laboratory lighting. The results of the present study indicate the important role of the antimony dopant species in the photonic activation process. The Sb^{4+} species can be formed if the electron generated by the photoionization of Ce^{3+} is trapped by a Sb^{5+} ion in the glass. The presence of Sb^{5+} ions in antimony containing silicate glass melts is expected based on detailed electrochemical studies characterizing the Sb^{3+}/Sb^{5+} redox equilibrium [29–31]. Direct evidence for Sb^{5+} in silicate glasses has also been given by Mössbauer spectroscopy [29,32].

In contrast none of the EPR spectra shown here give any evidence for the presence of unpaired electrons associated with silver atoms or Sn^{3+} species. Unpaired electrons associated with either Ag^0 or Ag^{2+} can be identified in the EPR spectra by the doublets resulting from the hyperfine interaction with the ^{107}Ag (nuclear spin $I = 1/2$, 51.8% abundant) and ^{109}Ag ($I = 1/2$, 48.2% abundant) nuclei. As documented in the literature, large nuclear hyperfine splitting is generally observed for atomic

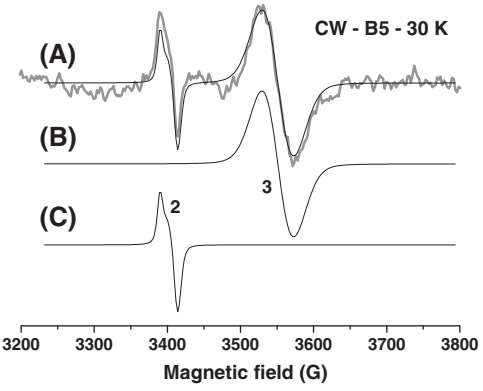

Fig. 4. Experimental cw spectrum of sample B5 (gray trace) and simulations (black traces). (A) Simulation with both anisotropic and isotropic components 2 and 3, respectively. (B—C) Isolated traces of simulated components 2 and 3. Microwave frequency: 9.475563 GHz.

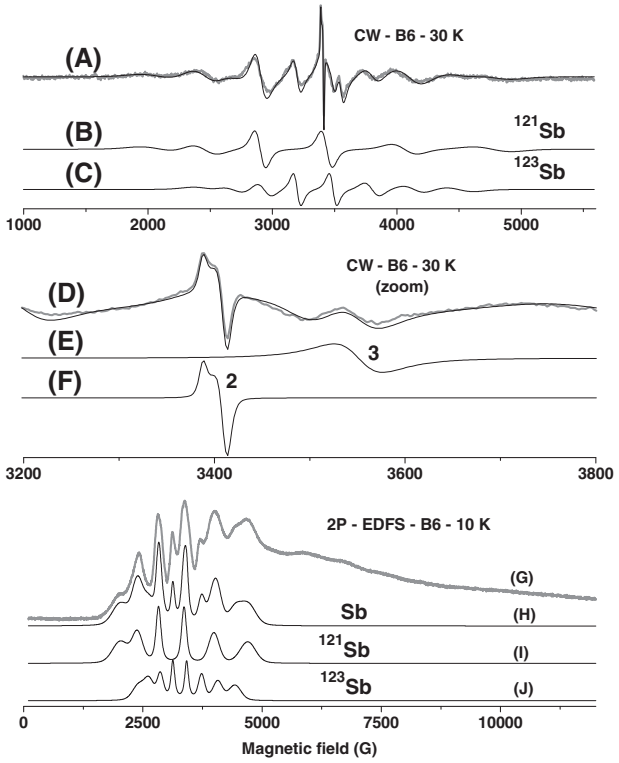

Fig. 5. Experimental cw and EDFS spectra of sample B6 (gray traces) and simulations (black traces). (A) Experimental and simulated cw-EPR spectra. (B) ^{121}Sb isotope component of simulated spectrum. (C) ^{123}Sb isotope component of simulated cw-EPR spectrum. (D–F) Zoom at the central part of the cw-EPR spectrum where components 2 and 3 can be visualized. (G) Experimental EDFS spectrum. (H—I) Simulations of the spectral component assigned to Sb^{4+} ions. Microwave frequency: 9.471313 GHz.

Ag [33,34] and small Ag_n^{m+} ($m < n$) clusters [35,36]. In addition, any EPR signals belonging to Sn^{3+} ions can be identified by satellite lines arising from nuclear hyperfine coupling with the spin-1/2 nuclear isotopes ^{117}Sn and ^{119}Sn (natural abundances of 7.6% and 8.6%) which have been observed for Sn^{3+} ions in inorganic matrices [37]. As none of such features are observed in the EPR spectra of our glasses the results of the present study offer no evidence for the direct involvement of Ag atoms or Sn^{3+} ions in the formation of unpaired electron species.

Based on the evidence presented here, we conclude that the electron generated by the photoionization of Ce^{3+} in the first step is not trapped by an Ag^+ ion but rather by a Sb^{5+} ion, resulting in the characteristic EPR signal of Sb^{4+}. The species remains rather transient, however, and disappears during the further annealing stages, which ultimately result in NaF crystallization. This is shown in Fig. 6, which reveals that all the photo-generated paramagnetic species (Sb^{4+}, along with the other two sharp features near $g = 1.9891$ and $g = 1.9063$) disappear upon thermal annealing. We may speculate that the electron is transferred further to Ag at this particular stage, resulting in the formation of larger silver clusters that do not give rise to a distinctive EPR lineshape. Together with the recent results from optical spectroscopy our results thus support the Nikonorov model [38,39] involving (1) photoionization of Ce^{3+}, (2) transfer of this electron to Sb^{5+} species to create a Sb^{4+} species, (3) upon annealing electron transfer from Sb^{4+} to Ag^+ ions, producing silver atoms, (4) coalescence of these species into Ag clusters, which (5) serve as nucleation catalysts for NaF nanocrystals.

4. Conclusions

Continuous-wave and pulsed electron spin echo resonance spectra obtained on UV-irradiated photo-thermal refractive glasses reveal a number of EPR active unpaired electron species, whose interaction parameters have been determined with the help of lineshape simulation

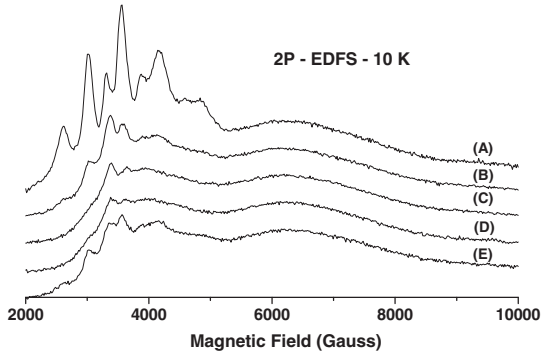

Fig. 6. Effect of thermal annealing upon the EDFS spectrum of PTR glass: From top to bottom: (A) sample B6, no annealing, (B) sample B6, annealed at 450 °C, 1 h, and at 520 °C, 2 h; (C) sample B6, annealed at 450 °C, 1 h, (D) sample B5, annealed at 450 °C, 1 h, (E) sample B5, no annealing.

routines. For detecting and characterizing the entire inventory of unpaired electrons generated during this process the combined use of continuous-wave and echo detected field sweep experiments turns out to be essential. The formation of Sb^{4+} species, which is characterized by a strong hyperfine interaction with the ^{121}Sb and ^{123}Sb nuclear isotopes is suggested to be a key step in the photo-activation process. Our results evidence that subsequent to the photoionization process of the Ce^{3+} ions, the electron is trapped by a nearby Sb^{5+} ion, resulting in the Sb^{4+} species. These findings corroborate the mechanism recently proposed by nikonorov's team. There is no direct EPR evidence for the formation of Ag^0 or small Ag_n^{m+} clusters upon photo-activation. The presence of various other paramagnetic species with *g*-values between 1.9 and 2.1 appears to be coincidental and most likely unrelated to the photothermal activation mechanism.

Acknowledgements

CJM, PDG, EDZ and HE acknowledge financial support by the Brazilian funding agencies São Paulo Research Foundation, FAPESP (CEPID Project 2013/07793-6) and CNPq (Universal Project 477053/2012-2 (HE)).

References

[1] L. Glebov, Proc. SPIE 6545 (2007) 654507.
[2] S.D. Stookey, D.H. Beall, J.E. Pierson, J. Appl. Phys. 49 (1978) 5114.
[3] O.M. Efimov, L.B. Glebov, L.N. Glebova, K.C. Richardson, V.I. Smirnov, Appl. Opt. 38 (1999) 619.
[4] O. M. Efimov, L. B. Glebov, V. I. Smirnov, L. Glebova, U.S: Patent Nr. 6,586,141 (2003).
[5] J.W. Zwanziger, U. Werner-Zwanziger, E.D. Zanotto, E. Rotari, L.N. Glebova, L.B. Glebov, J.F. Schneider, J. Appl. Phys. 99 (2006) 083511.
[6] L.B. Glebov, Opt. Mater. 25 (2004) 413.
[7] J. Lumeau, L. Glebova, V. Golubkov, E.D. Zanotto, L.B. Glebov, Opt. Mater. 32 (2009) 139.
[8] J. Lumeau, L. Glebova, L. Glebov, J. Non-Cryst. Solids 354 (2008) 425.
[9] L. Glebova, J. Lumeau, M. Klimov, E.D. Zanotto, L.B. Glebov, J. Non-Cryst. Solids 354 (2008) 456.
[10] J.S. Stroud, J. Chem. Phys. 35 (1961) 844.
[11] J. Lumeau, L. Glebova, L. Glebov, Opt. Mater. 36 (2014) 621–627.
[12] M. Anne, J. Lumeau, L. Glebova, L.B. Glebov, J. Non-Cryst. Solids 356 (2010) 2337.
[13] O.M. Efimov, A.I. Ignatiev, N.V. Nikonorov, E.S. Postnikov, J. Non-Cryst. Solids 357 (2011) 3500.
[14] O.M. Efimov, A.I. Ignatiev, N.V. Nikonorov, E.S. Postnikov, J. Non-Cryst. Solids 361 (2013) 26–37.
[15] E.M. Sgibnev, A.I. Ignatiev, N.V. Nikonorov, A.M. Efimov, E.S. Postnikov, J. Non-Cryst. Solids 378 (2013) 213.
[16] K. Chamma, J. Lumeau, L. Glebova, L.B. Glebov, J. Non-Cryst. Solids 356 (2010) 2363.
[17] O.M. Efimov, L.B. Glebov, H.P. Andre, Appl. Opt. 41 (2002) 1864.
[18] S. Stoll, A. Schweiger, EasySpin, a comprehensive software package for spectral simulation and analysis in {EPR}, J. Magn. Reson. 178 (2006) 42.
[19] D.L. Griscom, J. Non-Cryst. Solids 40 (1980) 211.
[20] E. Malchukova, B. Boizot, G. Petite, D. Ghaleb, Phys. Status Solidi C 4 (2007) 1280.
[21] C. Carnevali, M. Mattoni, F. Morazzoni, R. Scotti, M. Casu, A. Musinu, R. Krsmanovic, S. Polizzi, A. Speghini, M. Bettinelli, J. Am. Chem. Soc. 127 (2005) 14681.
[22] A. Bishay, C. Quadros, A. Piccini, Phys. Chem. Glasses 15 (1974) 109.
[23] M. Chiesa, K. Mattsson, S. Taccheo, T. Robin, L. Lablonde, D. Mechin, D. Milanese, J. Non-Cryst. Solids 403 (2014) 97.
[24] D. Möncke, D. Ehrt, Opt. Mater. 25 (2004) 425.
[25] D.L. Griscom, J. Non-Cryst. Solids 357 (2011) 1945.
[26] J.W.H. Schreurs, D.H. Davis, J. Chem. Phys. 71 (1979) 557.
[27] A.I. Aleksandrov, N.N. Bubnov, A.I. Prokof'ev, Appl. Magn. Reson. 9 (1995) 251.
[28] D. Möncke, D. Ehrt, J. Non-Cryst. Solids 345&346 (2004) 319.
[29] B. Stahlberg, B.D. Mosel, W. Müller-Warmuth, F.G.K. Baucke, Glastechn. Ber. Glass Sci. Technol. 61 (1988) 335.
[30] C. Rüssel, G. Gönna, J. Non-Cryst. Solids 260 (1999) 147.
[31] K.D. Kim, S.H. Lee, Ceramics-Silikáty 54 (2010) 14.
[32] W. Müller-Warmuth, H. Eckert, Phys. Rep. 88 (1982) 91 (and references therein).
[33] H. Hosono, J. Nishii, H. Kawazoe, T. Kanazawa, K. Ametani, J. Phys. Chem. 84 (1980) 2316.
[34] E.J. Friebele, D.L. Griscom, in: M. Tomozawa, R.H. Doremus (Eds.), Treatise on Materials Science and Technology, Glass II, 17, Academic Press, 1979.
[35] N.I. Mel'nikov, D.P. Peregood, R.A. Zhitnikov, J. Non-Cryst. Solids 16 (1974) 195.
[36] A.T. Brant, I.E. Halliburton, N.C. Giles, S.A. Basun, A. Grabar, D.R. Evans, J. Phys. Condens. Matter 25 (2013) 205501.
[37] B. Xu, L. Kevan, J. Phys. Chem. 95 (1991) 1147.
[38] S.A. Ivanov, N.V. Nikonorov, A.I. Ignatiev, Proc. 3rd Int. Conf. Photonics, Optics and Laser Technology (2015) 78.
[39] S.A. Ivanov, A.I. Ignatiev, N.V. Nikonorov, in: M. Hrabovsky, J.T. Sheridan, A. Fimia (Eds.),Holography, Advances and Modern Trends IV, Proc. SPIE 9508, 95080E, 2015, p. 1.